ARTICLES
https://doi.org/10.1038/s41567-019-0744-9
nature physics

Strong correlations and orbital texture in single-layer 1T-$TaSe_2$

Yi Chen[1,2,13], Wei Ruan[1,2,13], Meng Wu[1,2,13], Shujie Tang[3,4,5,6,7,13], Hyejin Ryu[5,8], Hsin-Zon Tsai[1,9], Ryan Lee[1], Salman Kahn[1], Franklin Liou[1], Caihong Jia[1,2,10], Oliver R. Albertini[11], Hongyu Xiong[3,4], Tao Jia[3,4], Zhi Liu[6], Jonathan A. Sobota[3,5], Amy Y. Liu[11], Joel E. Moore[1,2], Zhi-Xun Shen[3,4], Steven G. Louie[1,2], Sung-Kwan Mo[5] and Michael F. Crommie[1,2,12]*

Strong electron correlation can induce Mott insulating behaviour and produce intriguing states of matter such as unconventional superconductivity and quantum spin liquids. Recent advances in van der Waals material synthesis enable the exploration of Mott systems in the two-dimensional limit. Here we report characterization of the local electronic properties of single- and few-layer 1T-$TaSe_2$ via spatial- and momentum-resolved spectroscopy involving scanning tunnelling microscopy and angle-resolved photoemission. Our results indicate that electron correlation induces a robust Mott insulator state in single-layer 1T-$TaSe_2$ that is accompanied by unusual orbital texture. Interlayer coupling weakens the insulating phase, as shown by reduction of the energy gap and quenching of the correlation-driven orbital texture in bilayer and trilayer 1T-$TaSe_2$. This establishes single-layer 1T-$TaSe_2$ as a useful platform for investigating strong correlation physics in two dimensions.

Two-dimensional (2D) Mott insulators emerge when the Coulomb interaction (U) exceeds the bandwidth (W) in partially filled band systems that can be described by 2D Hubbard-like models[1]. Correlated electronic behaviour in quasi-2D Mott insulators leads to collective quantum phenomena[2,3] such as high-temperature superconductivity that is widely believed to arise through doping of Mott insulating copper–oxygen layers[4,5]. Certain stacked graphene systems have also recently been found to exhibit Mott-like insulating behaviour and unconventional superconductivity on gating[6–9]. Layered transition metal dichalcogenides offer another family of correlated quasi-2D materials, two examples being bulk 1T-TaS_2 and the surface of bulk 1T-$TaSe_2$, which have long been known to host unusual insulating phases in the star-of-David charge density wave (CDW) state[10–13]. Although widely believed to be Mott insulators[11,14,15], the insulating nature of these bulk systems is complicated by interlayer CDW stacking whose effects on the insulating phase remain controversial[16]. Interlayer hopping (which increases W) and interlayer dielectric screening (which decreases U) are expected to suppress Mott insulating behaviour[1,17,18], but orbital stacking has also been predicted to open a hybridization gap even in the absence of electron correlation[16,19,20].

Atomically thin 1T transition metal dichalcogenides offer an ideal platform to differentiate the contributions of electron correlation and interlayer effects in quasi-2D materials since single-layer systems can be fully characterized in the absence of interlayer coupling. Without interlayer coupling, the reduced screening environment of a single layer leads to increased Coulomb interaction and potentially enhanced correlation phenomena[21–25]. The effects of interlayer coupling can then be systematically determined by adding new layers to a material one at a time and mapping out the resulting stacking order and wavefunction properties. Previous studies on single-layer 1T-$NbSe_2$ and 1T-$TaSe_2$ have found unusual insulating behaviour[26,27], but electronic wavefunction texture and interlayer coupling effects were not examined. The nature of the insulating phase in these single-layer materials thus remains inconclusive.

Here we report a combined scanning tunnelling microscopy/spectroscopy (STM/STS), angle-resolved photoemission spectroscopy (ARPES), and theoretical study of the electronic structure of single-layer 1T-$TaSe_2$. Our results show that in the absence of interlayer coupling single-layer 1T-$TaSe_2$ hosts a Mott insulating ground state that exhibits a 109 ± 18 meV energy gap and unusual orbital texture. Bilayer and trilayer 1T-$TaSe_2$ with shifted stacking order exhibit successively smaller energy gaps and show no signs of the unusual orbital texture seen in the single-layer limit. The single-layer band structure and density of states of 1T-$TaSe_2$ are found to be consistent with density functional theory (DFT) + U calculations, confirming its Mott insulator nature. The unusual single-layer orbital texture, however, is not captured by DFT + U, but is consistent with the behaviour expected for a weakly screened, strongly correlated 2D insulator. Reduction of the 1T-$TaSe_2$ bandgap and quenching of the unusual orbital texture by the addition of new layers show that the effect of interlayer coupling on shifted-stacked

[1]Department of Physics, University of California, Berkeley, CA, USA. [2]Materials Sciences Division, Lawrence Berkeley National Laboratory, Berkeley, CA, USA. [3]Stanford Institute for Materials and Energy Sciences, SLAC National Accelerator Laboratory and Stanford University, Menlo Park, CA, USA. [4]Geballe Laboratory for Advanced Materials, Departments of Physics and Applied Physics, Stanford University, Stanford, CA, USA. [5]Advanced Light Source, Lawrence Berkeley National Laboratory, Berkeley, CA, USA. [6]CAS Center for Excellence in Superconducting Electronics, Shanghai Institute of Microsystem and Information Technology, Chinese Academy of Sciences, Shanghai, China. [7]School of Physical Science and Technology, Shanghai Tech University, Shanghai, China. [8]Center for Spintronics, Korea Institute of Science and Technology, Seoul, South Korea. [9]International Collaborative Laboratory of 2D Materials for Optoelectronic Science & Technology of Ministry of Education, Engineering Technology Research Center for 2D Material Information Function Devices and Systems of Guangdong Province, Shenzhen University, Shenzhen, China. [10]Henan Key Laboratory of Photovoltaic Materials and Laboratory of Low-dimensional Materials Science, School of Physics and Electronics, Henan University, Kaifeng, China. [11]Department of Physics, Georgetown University, Washington DC, USA. [12]Kavli Energy Nano Sciences Institute at the University of California Berkeley and the Lawrence Berkeley National Laboratory, Berkeley, CA, USA. [13]These authors contributed equally: Yi Chen, Wei Ruan, Meng Wu, Shujie Tang. *e-mail: crommie@berkeley.edu

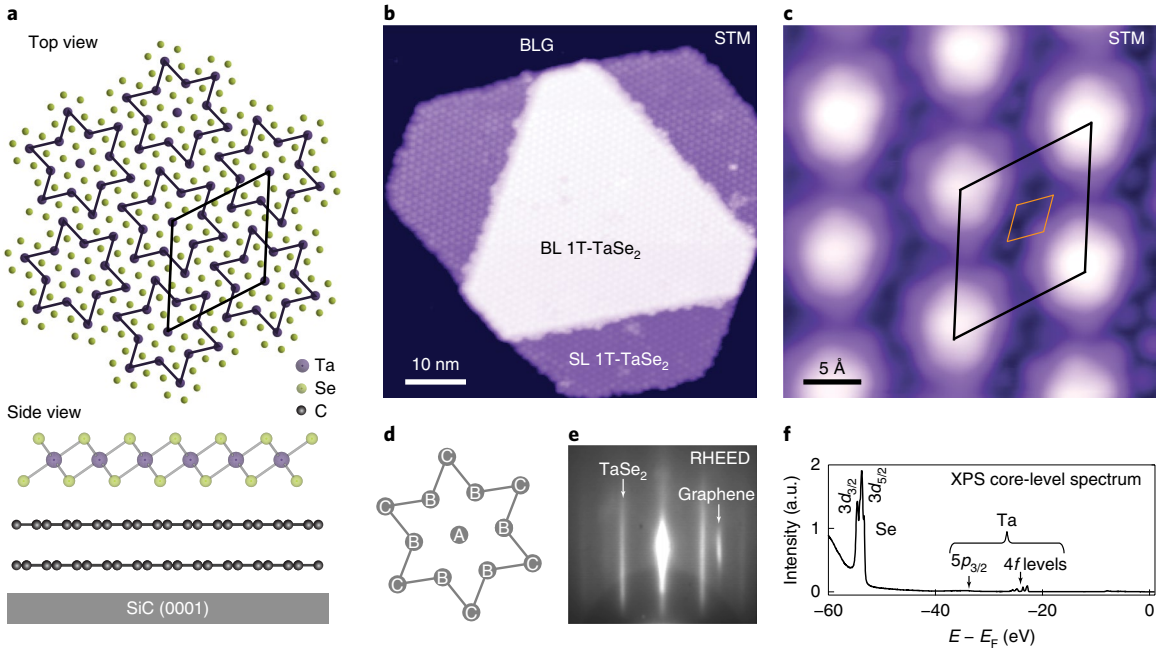

Fig. 1 | Structure of single-layer 1T-$TaSe_2$ in the star-of-David CDW phase. a, Top- and side-view sketches of single-layer 1T-$TaSe_2$, including the substrate. Clusters of 13 Ta atoms in star-of-David CDW supercells are outlined, as well as the CDW unit cell. **b**, A large-scale STM topograph of a typical 1T-$TaSe_2$ island shows single-layer (SL) and bilayer (BL) regions ($V_b = -0.5$ V, $I_t = 10$ pA, $T = 5$ K). **c**, A close-up STM image of single-layer 1T-$TaSe_2$. Each bright spot corresponds to a star-of-David supercell ($V_b = -0.17$ V, $I_t = 3$ nA, $T = 5$ K). The black and orange parallelograms mark CDW and atomic unit cells, respectively. **d**, Labels for Ta atoms in the star-of-David CDW supercell depend on the radial distance from the centre. **e**, The reflection high-energy electron diffraction (RHEED) pattern of a submonolayer 1T-$TaSe_2$ film. **f**, X-ray photoelectron spectroscopy (XPS) shows characteristic peaks of Ta and Se core levels for a submonolayer 1T-$TaSe_2$ film. a.u., arbitrary units.

1T-$TaSe_2$ is to weaken the Mott behaviour. The single-layer limit of 1T-$TaSe_2$ is thus unique in that strong correlation effects here are most pronounced, affecting both the energy gap and electron wavefunction symmetry.

Electronic structure of single-layer 1T-$TaSe_2$

Our experiments were carried out on 1T-$TaSe_2$ thin films grown by molecular beam epitaxy on epitaxial bilayer-graphene (BLG)-terminated 6H-SiC(0001), as sketched in Fig. 1a. The crystal structure of 1T-$TaSe_2$ consists of a layer of Ta atoms sandwiched between two layers of Se atoms in an octahedral coordination. Figure 1b illustrates the hexagonal morphology of our 1T-$TaSe_2$ islands, indicating high epitaxial growth quality. A triangular CDW superlattice is observed on single-layer, bilayer and trilayer 1T-$TaSe_2$, as seen in Fig. 1b,c and Supplementary Fig. 1 where each bright spot corresponds to a star-of-David CDW supercell. Fourier analysis of STM images (Supplementary Fig. 2) together with low-energy electron diffraction patterns (Supplementary Fig. 3) confirms the formation of a $\sqrt{13} \times \sqrt{13}$ CDW in single-layer 1T-$TaSe_2$, similar to the commensurate CDW phase of bulk 1T-$TaSe_2$ at $T < 473$ K (ref. [28]) (the atomic lattice and CDW superlattice are observed to have a relative rotation angle of approximately 13.9°). Reflection high-energy electron diffraction patterns (Fig. 1e) and X-ray photoelectron spectroscopy (Fig. 1f) show the structural and chemical integrity of our single-layer 1T-$TaSe_2$ samples (1T and 1H islands do coexist in our samples due to the metastability of 1T-$TaSe_2$ (Supplementary Fig. 4)).

We experimentally determined the electronic structure of single-layer 1T-$TaSe_2$ in the star-of-David CDW phase using ARPES and STS. Figure 2a,b shows the ARPES spectra of single-layer 1T-$TaSe_2$ for *p*- and *s*-polarized light, respectively, obtained at $T = 12$ K. At low binding energies, the single-layer 1T-$TaSe_2$ ARPES spectra show a strongly diminished intensity at all observed momenta, indicating insulating behaviour (some ARPES intensity from coexisting 1H-$TaSe_2$ islands can be seen crossing the Fermi level (E_F) at the wavevector $k \approx 0.5$ Å^{-1} (represented by white dashed lines)[29]). The CDW superlattice potential induces band folding into a smaller CDW Brillouin zone (Fig. 2b inset). One such band can be seen in the ARPES spectrum for *p*-polarized light (Fig. 2a) that shows a prominent flat band centred at $E - E_F \approx -0.26$ eV within the first CDW Brillouin zone (black dashed box). A more dispersive band can be resolved outside the first CDW Brillouin zone boundary (vertical dashed lines labelled A and B mark this boundary). These features have no obvious photon-energy dependence (Supplementary Fig. 5) and are similar to bands observed by ARPES at the surface of bulk samples of 1T-TaS_2 (refs. [16,30]) and 1T-$TaSe_2$ (ref. [12]). For *s*-polarized light (Fig. 2b), the flat band is much less visible and a manifold of highly dispersive bands near the Γ-point dominates the spectrum.

Our STM dI/dV spectrum (Fig. 3a (black curve)) confirms the insulating nature of single-layer 1T-$TaSe_2$. The electronic local density of states (LDOS) reflected in dI/dV exhibits a pronounced valence band peak at $V = -0.33$ V (labelled V_1) while dropping steeply at higher energy until reaching zero at $V \approx -0.05$ V. The zero LDOS region bracketing the Fermi level yields an energy gap of magnitude 109 ± 18 meV (see Supplementary Fig. 6 for gap determination). The experimental LDOS does not rise again until a narrow conduction band peak is observed centred at $V = 0.20$ V (labelled C_1) in the empty-state regime. The LDOS drops to zero again above the C_1 peak until higher-lying conduction band features are seen to rise at $V > 0.45$ V (for example, at C_2 and C_3). Aside from spatial variation in the relative peak heights, this gapped electronic structure is observed uniformly over the entire single-layer 1T-$TaSe_2$ surface (Supplementary Fig. 7). No significant band-bending effects are observed for different tip–sample separations (Supplementary

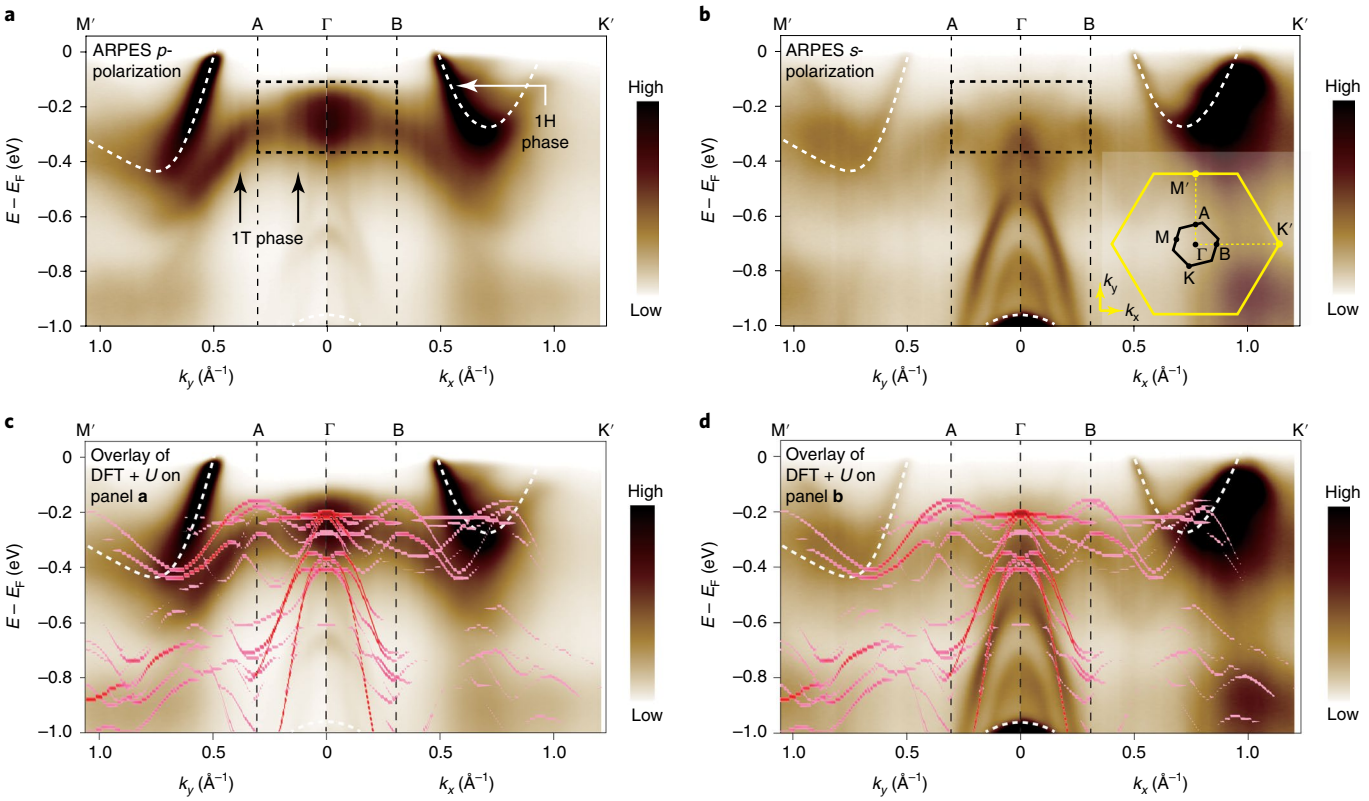

Fig. 2 | ARPES and DFT + *U* band structure of single-layer 1T-$TaSe_2$. a,b, ARPES spectra of single-layer 1T-$TaSe_2$ acquired with *p*-polarized (**a**) and *s*-polarized (**b**) light at $T = 12$ K along the Γ–K′ and Γ–M′ directions defined in the undistorted (that is, no CDW) unit cell Brillouin zone (yellow hexagon in Fig. 2b inset). ARPES spectra have little intensity at low binding energies except for coexisting 1H-$TaSe_2$ bands that cross E_F at $k \approx 0.5$ Å^{-1} (white dashed lines). A strong flat band is seen under *p*-polarized light in the first CDW Brillouin zone (black dashed box in **a**). The full CDW Brillouin zone is sketched in the inset of **b** (black hexagon). **c**, DFT + *U* band structure ($U = 2$ eV) of single-layer 1T-$TaSe_2$ unfolded onto the undistorted unit cell Brillouin zone compared to the ARPES spectrum under *p*-polarized light (from **a**). **d**, The same DFT + *U* band structure as in **c** compared to the ARPES spectrum under *s*-polarized light (from **b**).

Note 1 and Supplementary Figs. 8 and 9). To test substrate effects, we also grew single-layer 1T-$TaSe_2$ on cleaved graphite (HOPG), which shows similar STM spectra compared to single-layer 1T-$TaSe_2$/BLG (Supplementary Note 2 and Supplementary Fig. 10). This indicates that the small increase in screening provided by HOPG[21] (as shown by the slight downshift/upshift of empty-state/filled-state features in Supplementary Fig. 10) does not significantly change the 1T-$TaSe_2$ behaviour. We are so far unable to experimentally test the effect of reducing screening below the level provided by BLG.

Experimental orbital texture of single-layer 1T-$TaSe_2$

To gain additional insight into the insulating ground state of single-layer 1T-$TaSe_2$, we performed dI/dV spatial mapping of its energy-dependent orbital texture at constant tip–sample separation (Fig. 3b–h). dI/dV maps measured at negative biases all display a similar pattern where high-intensity LDOS is concentrated near the centre of each star-of-David (Fig. 3b,c and Supplementary Fig. 11). The experimental empty-state LDOS of single-layer 1T-$TaSe_2$, however, exhibits a completely different orbital texture. This is most clearly seen in the dI/dV map taken at the lowest conduction band peak C_1 (Fig. 3d) where the centre of each CDW supercell is observed to be dark with no LDOS intensity. At this energy, the LDOS exhibits an unusual, interlocked 'flower' pattern (circled by yellow dashed lines) consisting of six well-defined 'petals' (that is, bright spots) located around the outer rim of each star-of-David. This appearance is completely different from previous reports of conduction band LDOS in bulk 1T-$TaSe_2$ and 1T-TaS_2 (refs. [13,31]) (which show LDOS concentrated in the star-of-David centres), and is clearly not due to defects since it follows the CDW periodicity. The six-fold petal structure has a different symmetry from the three-fold arrangement of top-layer Se atoms in the spaces between each star-of-David, but it shares the six-fold symmetry of the Ta atom arrangement (Fig. 3a inset and Supplementary Fig. 12). Single-layer 1T-$TaSe_2$/HOPG shows a similar dI/dV map with the dominant LDOS intensity located near the outer rim of the stars-of-David at the lowest conduction band peak (dI/dV maps at other energies also look similar, see Supplementary Fig. 10 and Supplementary Note 2).

The dI/dV map of single-layer 1T-$TaSe_2$/BLG obtained at a slightly higher bias of $V = 0.6$ V (C_2) shows LDOS that is related to the flower pattern in that it exhibits a nearly inverse flower (so that the dark areas at C_1 are bright at C_2, see circled regions in Fig. 3e). At even higher energies, the single-layer 1T-$TaSe_2$ LDOS displays other intricate orbital textures. The map at 0.8 V (Fig. 3f), for example, shows quasi-triangular patterns with intensity distributed near the outermost Ta C atoms (labelled according to the convention shown in Fig. 1d). This evolves into trimer-like features at 1.1 V (Fig. 3g), and a network of 'rings' with intensity near Ta B atoms at $V = 1.2$ V (Fig. 3h) (a complete set of constant-height dI/dV maps is shown in Supplementary Fig. 11).

To help quantify the complex energy-dependent LDOS distribution of single-layer 1T-$TaSe_2$, we cross-correlated our dI/dV maps with a reference map taken at the maximum of the valence band peak V_1 (Fig. 3c), which exhibits LDOS dominated by inner Ta A and B atoms. The resulting cross-correlation values are colour-coded in Fig. 3a and show that occupied states ($-1\,\text{V} < V < 0\,\text{V}$) all have a strong, positive cross-correlation (blue) with the valence

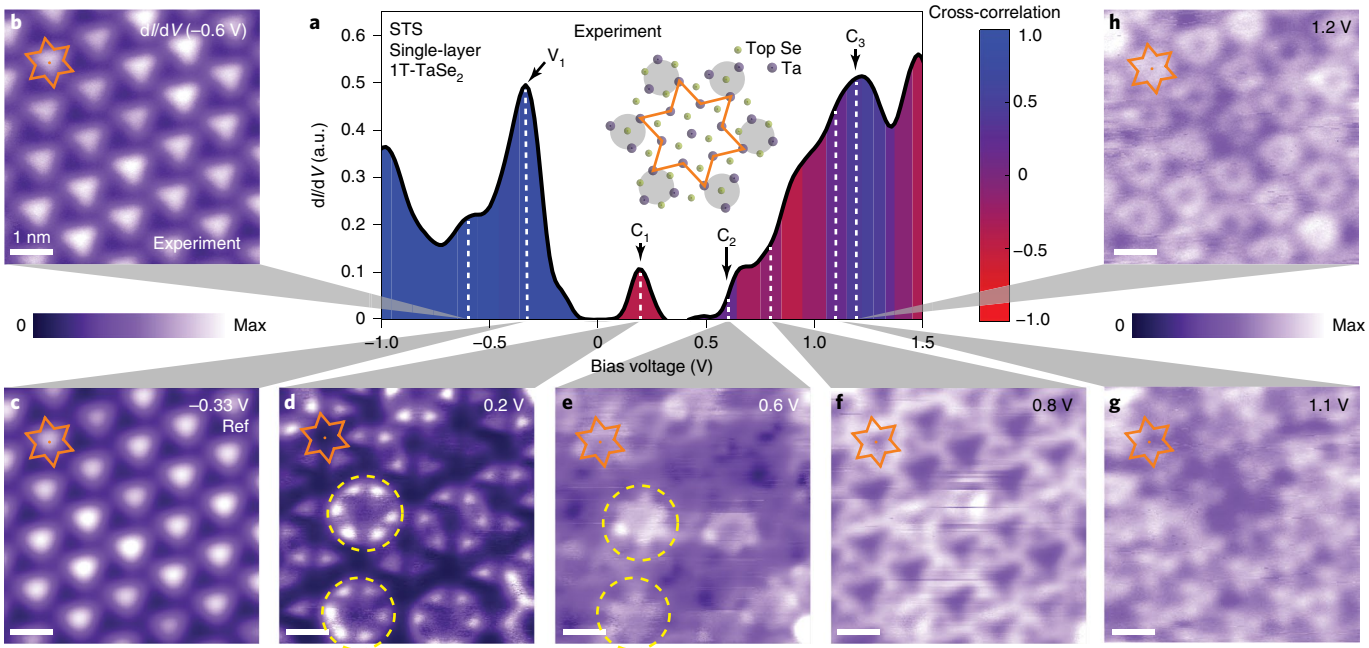

Fig. 3 | Experimental energy-resolved unusual orbital texture of single-layer 1T-$TaSe_2$. **a**, The STM d*I*/d*V* spectrum of single-layer 1T-$TaSe_2$ shows a full energy gap bracketed by two STS peaks labelled V_1 and C_1 ($f = 401$ Hz, $I_t = 50$ pA, $V_{r.m.s.} = 20$ mV). The colour shows cross-correlation of d*I*/d*V* maps at different energies with the reference map shown in **c**. The inset shows how the unusual orbital texture in **d** compares to atomic site locations (the six-fold petal structure is shaded grey in the inset). **b**–**h**, Constant-height d*I*/d*V* conductance maps of the same area for different bias voltages show energy-dependent orbital texture ($f = 401$ Hz, $V_{r.m.s.} = 20$ mV). The same star-of-David CDW supercell is outlined in each map (orange line). The yellow dashed circles in **d** and **e** highlight the unusual LDOS patterns at C_1 and C_2 and their relative spatial inversion.

band map at V_1 (so that the central Ta A and B atoms are bright at these energies and the C atoms are darker). The empty-state cross-correlation, however, is very different. At C_1 (where the flower pattern is observed), the LDOS map is strongly anti-correlated (red) with the valence band map since the LDOS here is dominated by Ta C atoms. At slightly higher energy (C_2), the cross-correlation flips to blue. This is due to the LDOS inversion that occurs at the energy of the inverse flower pattern and that creates intensity at the interior A and B atoms. At higher energy, the cross-correlation flips again to red and stays red over a fairly wide energy range (~0.4 eV) before flipping again to blue near C_3.

Energy gap and orbital texture in few-layer 1T-$TaSe_2$

We examined the effect of interlayer coupling on 1T-$TaSe_2$ by studying the evolution in electronic structure as 1T-$TaSe_2$ is stacked layer by layer. We first determined the star-of-David CDW stacking order for bilayer and trilayer 1T-$TaSe_2$. As seen in the STM images of Fig. 1b and Supplementary Fig. 1, the CDW stacking order follows the shifted triclinic structure whereby inner Ta A atoms sit on top of outer Ta C atoms, similar to stacking observed in bulk 1T-$TaSe_2$ (ref. [32]). We observe that the energy gap for 1T-$TaSe_2$ narrows significantly when interlayer coupling is added, as seen in the STM d*I*/d*V* spectra for bilayer and trilayer 1T-$TaSe_2$ shown in Fig. 4a. The bilayer energy gap reduces to 21 ± 8 meV while trilayer 1T-$TaSe_2$ shows a reduction in LDOS at E_F that can be described as 'semimetallic' but exhibits no true energy gap.

In addition to reducing the 1T-$TaSe_2$ energy gap, bilayer and trilayer formation also quench the unusual orbital texture observed in the single-layer limit. As shown in the insets to Fig. 4b,c, d*I*/d*V* maps of the lowest conduction band in bilayer and trilayer 1T-$TaSe_2$ show LDOS intensity concentrated near the centre of each star-of-David, in contrast to the flower-like orbital texture observed in single-layer 1T-$TaSe_2$ at C_1. This difference can also be seen in the colour-coded cross-correlation values of bilayer and trilayer 1T-$TaSe_2$ (Fig. 4b,c). Using the valence band LDOS shown in the insets as a reference (which is similar to the single-layer valence band LDOS of Fig. 3c), the bilayer and trilayer cross-correlation remain strongly positive (blue) throughout the lowest conduction band (thus, emphasizing that the LDOS here is concentrated on the interior Ta A and B atoms). The distinctive flower pattern seen in single-layer 1T-$TaSe_2$ at C_1 (Fig. 3d) is never seen in bilayer or trilayer LDOS at any bias (Supplementary Figs. 13 and 14).

Theoretical electronic structure of single-layer 1T-$TaSe_2$

There are two main physical questions that we seek to answer regarding our measurements of single- and few-layer 1T-$TaSe_2$. First, what type of insulator is single-layer 1T-$TaSe_2$? Second, what is the effect of interlayer coupling on 1T-$TaSe_2$ electronic behaviour as new layers are added? To address these questions, we first performed a conventional band-structure calculation for freestanding single-layer 1T-$TaSe_2$ using DFT. From an intuitive perspective, single-layer 1T-$TaSe_2$ is expected to have metallic band structure since there are an odd number of Ta ions in the star-of-David unit cell (13) and each Ta^{4+} ion has only one *d*-electron (in principle, substrate charge transfer could alter the electron counting and/or the CDW behaviour[33], but in our case charge transfer effects from the graphene substrate are negligible (Supplementary Fig. 15 and Supplementary Note 3)). As expected, the DFT band structure of single-layer 1T-$TaSe_2$ in the CDW phase calculated using the Perdew–Burke–Ernzerhof (PBE) exchange correlation functional shows a metallic half-filled band at E_F (Supplementary Fig. 16). This theoretical result, however, disagrees with our experimental data that show insulating behaviour for single-layer 1T-$TaSe_2$ (Figs. 2 and 3). An explanation for this discrepancy is that since the metallic band is so narrow (only approximately 20 meV wide), it is unstable and may lead to splitting into lower and upper Hubbard bands

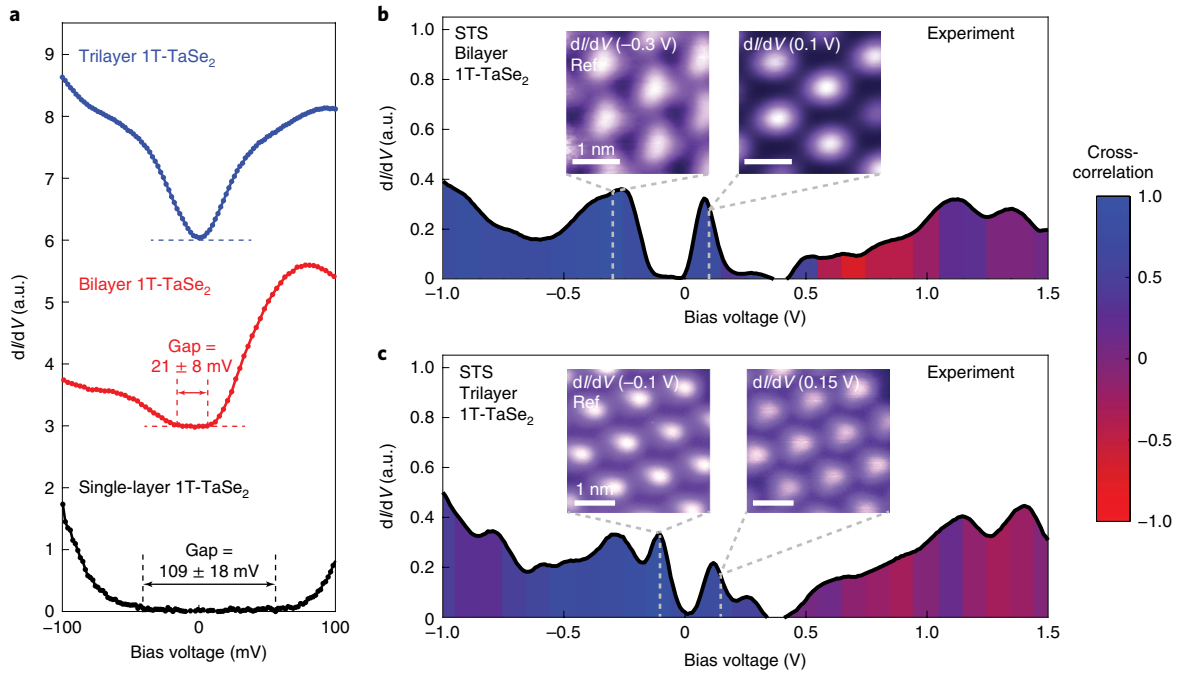

Fig. 4 | Energy gap reduction and quenching of unusual orbital texture in few-layer 1T-$TaSe_2$. **a**, STM d*I*/d*V* spectra for single-layer, bilayer and trilayer 1T-$TaSe_2$ show how interlayer coupling reduces the energy gap with an increasing number of layers. The spectra are shifted vertically for viewing (the horizontal dashed lines mark d*I*/d*V* = 0, f = 401 Hz, $V_{r.m.s.}$ = 2 mV). **b**,**c**, d*I*/d*V* maps of the valence and conduction band LDOS as well as larger energy-scale d*I*/d*V* spectra of bilayer (**b**) and trilayer (**c**) 1T-$TaSe_2$ (f = 401 Hz, $V_{r.m.s.}$ = 20 mV). Spatial cross-correlation values are shown colour-coded with references taken near the LDOS maximum of the valence band for bilayer and trilayer 1T-$TaSe_2$. In contrast to single-layer 1T-$TaSe_2$, the lowest conduction band for both bilayer and trilayer shows no unusual orbital texture, thus resulting in positive cross-correlation values (blue), indicating that LDOS is concentrated on the interior Ta A and B atoms.

(LHB and UHB) due to a high on-site Coulomb energy (U). This is the condition that causes Mott insulators to arise from otherwise metallic phases[1].

To test for Mott insulator formation in single-layer 1T-$TaSe_2$, we modelled the effects of electron correlation by performing DFT + U simulations. We find that the DFT + U band structure for a ferromagnetic ground state with U = 2 eV reproduces most of our experimentally observed electronic structure for single-layer 1T-$TaSe_2$ (the DFT + U results were sensitive to neither the magnetic ground state nor the structural optimization conditions, and our U value is consistent with previous simulations of related systems[31,34,35] (see Supplementary Note 4 and Supplementary Figs. 17–21)). We first compared the DFT + U band structure to our ARPES data by unfolding it onto the Brillouin zone of an undistorted unit cell. As seen in Fig. 2c,d and Supplementary Fig. 22, it reproduces the gapped electronic structure and shows good overall agreement with the ARPES spectra. In particular, DFT + U predicts that the LHB at −0.2 eV originates mainly from Ta d_{z^2} orbitals, consistent with the higher ARPES intensity under p-polarized light (Fig. 2a)[36].

The DFT + U simulations are also consistent with much of our STS data as shown in Fig. 5, which displays the simulated density-of-states spectrum and LDOS maps for single-layer 1T-$TaSe_2$. The theoretical density-of-states spectrum (Fig. 5a, black line) reproduces the d*I*/d*V* spectrum (Fig. 3a) reasonably well in both the occupied and empty states. A LHB corresponding to the experimental V_1 feature is seen, as well as an UHB corresponding to C_1, along with higher-energy features that correspond to the experimental C_2 and C_3 features. The orbital textures generated by the DFT + U calculations (Fig. 5b–h) also agree well with the experimental d*I*/d*V* maps in the valence band and upper conduction band regimes (meaning energies corresponding to filled states and levels above C_2).

However, there are significant discrepancies between the experimental and theoretical LDOS maps in the low-energy conduction band region ($0 < E \lesssim 0.6$ eV) where the unusual orbital texture is observed experimentally. This is most clearly seen by comparing the theoretical UHB LDOS map at 0.2 eV (Fig. 5d) with the experimental d*I*/d*V* map at V = 0.2 V (Fig. 3d) (the energy corresponding to C_1). The calculated LDOS has high intensity in the central Ta A and B atom regions (similar to what is seen in the LHB) while the experiment shows the flower pattern (that is, the experimental LDOS occupies the Ta C atom region and is dark in the central area). There also exists significant disagreement at the next higher energy band feature (C_2), as seen by comparison of Figs. 3e and 5e. Here the theoretical orbital texture (Fig. 5e) shows propeller-like structures with low central LDOS intensity, while the experimental d*I*/d*V* map (Fig. 3e) shows an inverse of the C_1 flower pattern with high LDOS intensity in the interior region of the star-of-David (a complete set of theoretical LDOS maps is shown in Supplementary Fig. 23).

Unusual empty-state orbital texture at C_1 and C_2

The good agreement between our DFT + U simulations and the majority of our ARPES and STM/STS data provides strong evidence that single-layer 1T-$TaSe_2$ is a 2D Mott insulator. However, the failure of the simulations to reproduce the unusual conduction band orbital texture at C_1/C_2 implies that additional electron–electron interactions occur in single-layer 1T-$TaSe_2$ that are not captured by DFT + U. Electrons injected from the STM tip into single-layer 1T-$TaSe_2$ at the C_1/C_2 energies experience additional correlation effects originating from their Coulomb interaction with electrons already present in the occupied electronic states. Such behaviour is expected to arise due to the LHB charge distribution (Fig. 3c) that creates a spatially varying Coulomb repulsion landscape, $\tilde{U}(r)$, felt

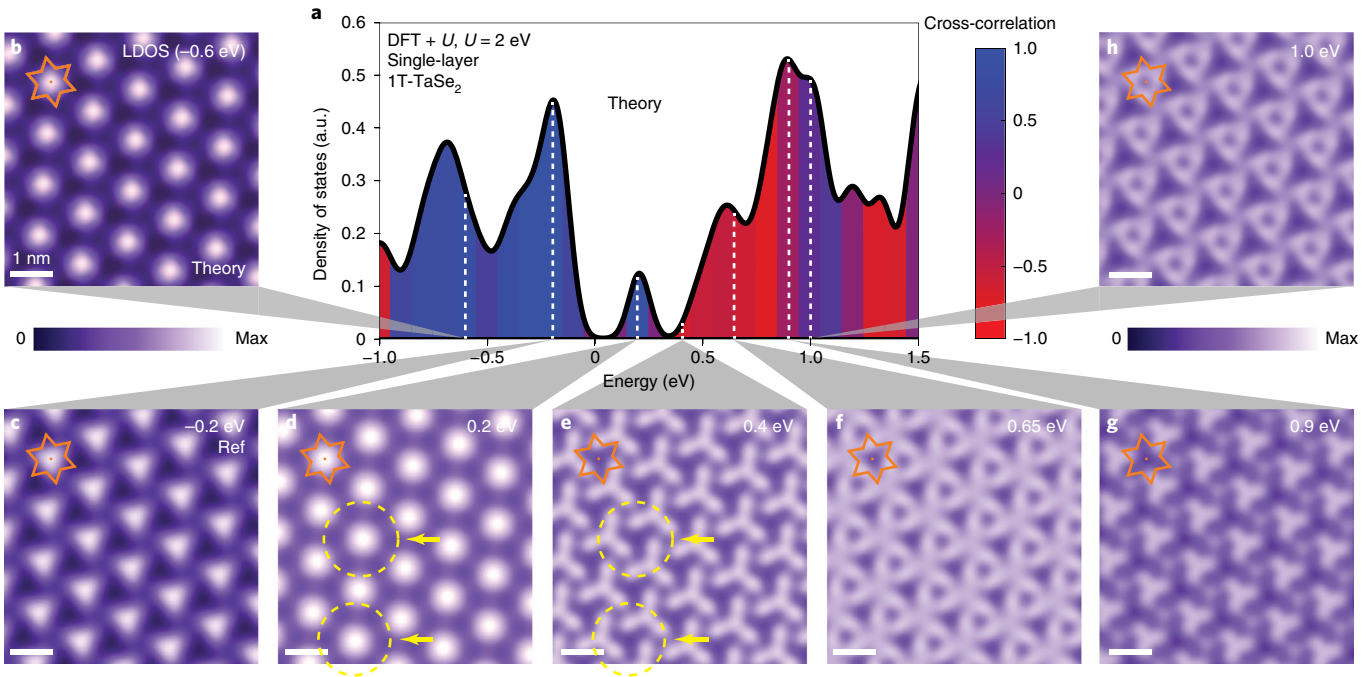

Fig. 5 | Theoretical orbital texture of single-layer 1T-$TaSe_2$ from DFT + *U* simulations. a, The theoretical density of states of single-layer 1T-$TaSe_2$ from DFT + *U* simulations (*U* = 2 eV). The colour shows cross-correlation of LDOS maps at different energies with respect to the reference map in **c** (−0.2 eV). **b**–**h**, Theoretical LDOS maps of single-layer 1T-$TaSe_2$ from DFT + *U* simulations (*U* = 2 eV). The same star-of-David supercell is outlined in each map (orange line). The yellow dashed circles in **d** and **e** highlight two star-of-David clusters that show very different theoretical conduction band orbital textures compared to the experimental C_1 and C_2 features in Fig. 3d,e.

preferentially by electrons injected into UHB states since they share a common orbital. $\tilde{U}(r)$ can be estimated by treating the LHB as a Gaussian charge distribution within each star-of-David cluster and by calculating the resulting interaction energy (Supplementary Note 5). This leads to a Coulomb landscape (Supplementary Fig. 24) that is strongly repulsive to UHB electrons at the centre of each star-of-David (where the LHB charge density is high) and that has minima at precisely the locations of the six-fold C_1 flower petals (where the LHB charge density is low). Given the composite nature of the UHB orbital (which has contributions from 13 Ta atoms over the CDW cell), the unusual orbital texture at C_1/C_2 can thus be understood as a redistribution of the UHB spectral density at the centre of each star-of-David up to higher energy in response to enhanced Coulomb interactions that arise from reduced screening in two dimensions. The remaining state density of the composite UHB stays in the $\tilde{U}(r)$ minima regions and gives rise to the peripheral six-fold C_1 flower petals. This picture is corroborated by our observation that on the more strongly screened graphite substrate the LDOS distribution at C_1 of single-layer 1T-$TaSe_2$ appears to be more smeared out around the outer rim of the star-of-David cells, consistent with a less corrugated $\tilde{U}(r)$ landscape (Supplementary Fig. 10 and Supplementary Note 2). Future theoretical treatments considering dynamical interactions could potentially provide more insight into this unusual strong correlation phenomenon.

The effect of interlayer coupling on the shifted-stacked 1T-$TaSe_2$ electronic structure is to weaken the Mott insulator phase, as seen by both the observed energy gap reduction with increased layer number and the effect on orbital texture. The bilayer and trilayer orbital textures, for example, show no signs of the correlation-induced spectral density shift seen in the single-layer material at C_1/C_2. Such weakening of the Mott behaviour probably arises from an increase in the effective inter-star-of-David hopping parameter (*t*) of the bilayer and trilayer due to interlayer coupling, as well as a reduction in Coulomb interactions due to increased electronic delocalization and screening.

Outlook

We have shown that single-layer 1T-$TaSe_2$ is a strongly correlated 2D Mott insulator characterized by unusual orbital texture. Interlayer coupling weakens the Mott behaviour, consistent with the evolution of 1T-$TaSe_2$ into a metal as its thickness is increased layer by layer. The Mott insulator phase seen in single-layer 1T-$TaSe_2$ thus offers a highly tunable 2D platform for future exploration of metal–insulator transitions[1] where the Coulomb interaction might be further modified by substrate screening[21,37], the bandwidth by pressure[38], or the carrier density by electrostatic gating[6,8].

Online content

Any methods, additional references, Nature Research reporting summaries, source data, extended data, supplementary information, acknowledgements, peer review information; details of author contributions and competing interests; and statements of data and code availability are available at https://doi.org/10.1038/s41567-019-0744-9.

Received: 23 April 2019; Accepted: 8 November 2019;
Published online: 6 January 2020

References

1. Imada, M., Fujimori, A. & Tokura, Y. Metal–insulator transitions. *Rev. Mod. Phys.* **70**, 1039–1263 (1998).
2. Keimer, B. & Moore, J. E. The physics of quantum materials. *Nat. Phys.* **13**, 1045–1055 (2017).
3. Kravchenko, S. *Strongly Correlated Electrons in Two Dimensions* (Pan Stanford, 2017).
4. Dagotto, E. Correlated electrons in high-temperature superconductors. *Rev. Mod. Phys.* **66**, 763–840 (1994).

5. Lee, P. A., Nagaosa, N. & Wen, X.-G. Doping a Mott insulator: physics of high-temperature superconductivity. *Rev. Mod. Phys.* **78**, 17–85 (2006).
6. Cao, Y. et al. Correlated insulator behaviour at half-filling in magic-angle graphene superlattices. *Nature* **556**, 80–84 (2018).
7. Cao, Y. et al. Unconventional superconductivity in magic-angle graphene superlattices. *Nature* **556**, 43–50 (2018).
8. Chen, G. et al. Evidence of a gate-tunable Mott insulator in a trilayer graphene moiré superlattice. *Nat. Phys.* **15**, 237–241 (2019).
9. Chen, G. et al. Signatures of tunable superconductivity in a trilayer graphene moiré superlattice. *Nature* **572**, 215–219 (2019).
10. Wilson, J. A. & Yoffe, A. D. The transition metal dichalcogenides discussion and interpretation of the observed optical, electrical and structural properties. *Adv. Phys.* **18**, 193–335 (1969).
11. Fazekas, P. & Tosatti, E. Electrical, structural and magnetic properties of pure and doped 1T-TaS_2. *Philos. Mag. B* **39**, 229–244 (1979).
12. Perfetti, L. et al. Spectroscopic signatures of a bandwidth-controlled Mott transition at the surface of 1T-$TaSe_2$. *Phys. Rev. Lett.* **90**, 166401 (2003).
13. Colonna, S. et al. Mott phase at the surface of 1T-$TaSe_2$ observed by scanning tunneling microscopy. *Phys. Rev. Lett.* **94**, 036405 (2005).
14. Tosatti, E. & Fazekas, P. On the nature of the low-temperature phase of 1T-TaS_2. *J. Phys. Colloq.* **37**, 165–168 (1976).
15. Sipos, B. et al. From Mott state to superconductivity in 1T-TaS_2. *Nat. Mater.* **7**, 960–965 (2008).
16. Ritschel, T. et al. Orbital textures and charge density waves in transition metal dichalcogenides. *Nat. Phys.* **11**, 328–331 (2015).
17. Ma, L. et al. A metallic mosaic phase and the origin of Mott-insulating state in 1T-TaS_2. *Nat. Commun.* **7**, 10956 (2016).
18. Cho, D. et al. Nanoscale manipulation of the Mott insulating state coupled to charge order in 1T-TaS_2. *Nat. Commun.* **7**, 10453 (2016).
19. Ritschel, T., Berger, H. & Geck, J. Stacking-driven gap formation in layered 1T-TaS_2. *Phys. Rev. B* **98**, 195134 (2018).
20. Lee, S.-H., Goh, J. S. & Cho, D. Origin of the insulating phase and first-order metal–insulator transition in 1T-TaS_2. *Phys. Rev. Lett.* **122**, 106404 (2019).
21. Ugeda, M. M. et al. Giant bandgap renormalization and excitonic effects in a monolayer transition metal dichalcogenide semiconductor. *Nat. Mater.* **13**, 1091–1095 (2014).
22. He, K. et al. Tightly bound excitons in monolayer WSe_2. *Phys. Rev. Lett.* **113**, 026803 (2014).
23. Qiu, D. Y., da Jornada, F. H. & Louie, S. G. Screening and many-body effects in two-dimensional crystals: monolayer MoS_2. *Phys. Rev. B* **93**, 235435 (2016).
24. Halperin, B. I. & Rice, T. M. Possible anomalies at a semimetal–semiconductor transistion. *Rev. Mod. Phys.* **40**, 755–766 (1968).
25. Narozhny, B. N. & Levchenko, A. Coulomb drag. *Rev. Mod. Phys.* **88**, 025003 (2016).
26. Nakata, Y. et al. Monolayer 1T-$NbSe_2$ as a Mott insulator. *NPG Asia Mater.* **8**, e321 (2016).
27. Nakata, Y. et al. Selective fabrication of Mott-insulating and metallic monolayer $TaSe_2$. *ACS Appl. Nano Mater.* **1**, 1456–1460 (2018).
28. Di Salvo, F. J., Maines, R. G., Waszczak, J. V. & Schwall, R. E. Preparation and properties of 1T-$TaSe_2$. *Solid State Commun.* **14**, 497–501 (1974).
29. Ryu, H. et al. Persistent charge-density-wave order in single-layer $TaSe_2$. *Nano Lett.* **18**, 689–694 (2018).
30. Sohrt, C., Stange, A., Bauer, M. & Rossnagel, K. How fast can a Peierls–Mott insulator be melted? *Faraday Discuss.* **171**, 243–257 (2014).
31. Qiao, S. et al. Mottness collapse in 1T−$TaS_{2-x}Se_x$ transition-metal dichalcogenide: an interplay between localized and itinerant orbitals. *Phys. Rev. X* **7**, 041054 (2017).
32. Brouwer, R. & Jellinek, F. The low-temperature superstructures of 1T-$TaSe_2$ and 2H-$TaSe_2$. *Phys. B+C* **99**, 51–55 (1980).
33. Sanders, C. E. et al. Crystalline and electronic structure of single-layer TaS_2. *Phys. Rev. B* **94**, 081404 (2016).
34. Darancet, P., Millis, A. J. & Marianetti, C. A. Three-dimensional metallic and two-dimensional insulating behavior in octahedral tantalum dichalcogenides. *Phys. Rev. B* **90**, 045134 (2014).
35. Yu, X.-L. et al. Electronic correlation effects and orbital density wave in the layered compound 1T-TaS_2. *Phys. Rev. B* **96**, 125138 (2017).
36. Moser, S. An experimentalist's guide to the matrix element in angle resolved photoemission. *J. Electron Spectrosc.* **214**, 29–52 (2017).
37. Qiu, Z. et al. Giant gate-tunable bandgap renormalization and excitonic effects in a 2D semiconductor. *Sci. Adv.* **5**, eaaw2347 (2019).
38. Yankowitz, M. et al. Dynamic band-structure tuning of graphene moiré superlattices with pressure. *Nature* **557**, 404–408 (2018).

Methods

Sample growth and ARPES measurements. Single-layer 1T-$TaSe_2$ films were grown on epitaxial BLG-terminated 6H-SiC(0001) and cleaved HOPG substrates in a molecular beam epitaxy chamber operating at ultrahigh vacuum (UHV, base pressure 2×10^{-10} torr) at the HERS endstation of Beamline 10.0.1, Advanced Light Source, Lawrence Berkeley National Laboratory. High-purity Ta (99.9%) and Se (99.999%) were evaporated from an electron-beam evaporator and a standard Knudsen cell, respectively, with a Ta/Se flux ratio set between 1:10 and 1:20 and a substrate temperature of 660 °C. A higher substrate temperature (compared with our previous 1H-$TaSe_2$ growth at 550 °C[29]) was used to facilitate the growth of the metastable 1T phase of $TaSe_2$. The growth process was monitored by reflection high-energy electron diffraction. After growth, the films were transferred in situ into the analysis chamber (base pressure 3×10^{-11} torr) for ARPES and core-level spectra measurements. The ARPES system was equipped with a Scienta R4000 electron analyser. The photon energy was set at 51 eV (unless specified otherwise) with an energy and angular resolution of 12 meV and 0.1°, respectively. *p*- and *s*-polarized light were used, as described elsewhere (ref. [39]). Before taking the films out of vacuum for STM/STS measurements, Se capping layers with ~10 nm thickness were deposited onto the samples for protection. These were later removed by UHV annealing at ~200 °C for 3 h.

STM/STS measurements. STM/STS measurements were performed using a commercial CreaTec STM/AFM system at $T=5$ K under UHV conditions. To avoid tip artefacts, STM tips were calibrated on a Au(111) surface by measuring its herringbone surface reconstruction and Shockley surface state before all STM/STS measurements. Both W and Pt–Ir STM tips were used and yielded similar results. STM dI/dV spectra were obtained using standard lock-in techniques with a small bias modulation at 401 Hz. The constant-height mode (that is, feedback loop open) was used for collecting all dI/dV conductance maps. Before obtaining each set of maps, the STM tip was parked near the sample surface for at least 8 h to minimize piezoelectric drift effects.

Electronic structure calculations. First-principles calculations of single-layer 1T-$TaSe_2$ were performed using DFT as implemented in the Quantum ESPRESSO package[40]. The onsite Hubbard interaction was added through the simplified rotationally invariant approach using the same U value for each Ta atom[41,42]. A slab model with a 16 Å vacuum layer was adopted to avoid interactions between periodic images. We employed optimized norm-conserving Vanderbilt pseudopotentials including Ta 5*s* and 5*p* semicore states (with a plane-wave energy cutoff of 90 Ry)[43–45] as well as the PBE exchange-correlation functional[46] in the generalized gradient approximation. The structure was fully relaxed at the DFT–PBE level until the force on each atom was less than 0.02 eV Å^{-1} (unless specified otherwise). The resulting relaxed single-layer 1T-$TaSe_2$ in the $\sqrt{13}\times\sqrt{13}$ CDW phase has a lattice constant of $a=12.63$ Å. Spin–orbit coupling was not taken into account in our calculations since it has a negligible influence on the band structure given the inversion symmetry of this system. The unfolding of the band structure from the CDW supercell to the undistorted unit cell was calculated using the BandUP code[47,48] with band energies and wavefunctions obtained from the Quantum ESPRESSO package.

Data availability

The data represented in Figs. 1f, 3a, 4 and 5a are available with the paper. All other data that support the plots within this paper and other findings of this study are available from the corresponding author upon reasonable request.

Code availability

The codes used in this study are available from the corresponding author upon reasonable request.

References

39. Tang, S. et al. Quantum spin Hall state in monolayer 1T′-WTe_2. *Nat. Phys.* **13**, 683–687 (2017).
40. Giannozzi, P. et al. QUANTUM ESPRESSO: a modular and open-source software project for quantum simulations of materials. *J. Phys. Condens. Matter* **21**, 395502 (2009).
41. Liechtenstein, A. I., Anisimov, V. I. & Zaanen, J. Density-functional theory and strong interactions: orbital ordering in Mott–Hubbard insulators. *Phys. Rev. B* **52**, R5467–R5470 (1995).
42. Dudarev, S. L., Botton, G. A., Savrasov, S. Y., Humphreys, C. J. & Sutton, A. P. Electron-energy-loss spectra and the structural stability of nickel oxide: an LSDA+U study. *Phys. Rev. B* **57**, 1505–1509 (1998).
43. Hamann, D. R. Optimized norm-conserving Vanderbilt pseudopotentials. *Phys. Rev. B* **88**, 085117 (2013).
44. Schlipf, M. & Gygi, F. Optimization algorithm for the generation of ONCV pseudopotentials. *Comput. Phys. Commun.* **196**, 36–44 (2015).
45. Scherpelz, P., Govoni, M., Hamada, I. & Galli, G. Implementation and validation of fully relativistic GW calculations: spin–orbit coupling in molecules, nanocrystals, and solids. *J. Chem. Theory Comput.* **12**, 3523–3544 (2016).
46. Perdew, J. P., Burke, K. & Ernzerhof, M. Generalized gradient approximation made simple. *Phys. Rev. Lett.* **77**, 3865–3868 (1996).
47. Medeiros, P. V. C., Stafström, S. & Björk, J. Effects of extrinsic and intrinsic perturbations on the electronic structure of graphene: retaining an effective primitive cell band structure by band unfolding. *Phys. Rev. B* **89**, 041407 (2014).
48. Medeiros, P. V. C., Tsirkin, S. S., Stafström, S. & Björk, J. Unfolding spinor wave functions and expectation values of general operators: introducing the unfolding-density operator. *Phys. Rev. B* **91**, 041116 (2015).

Acknowledgements

We thank P.A. Lee and D.-H. Lee for helpful discussions. This research was supported by the VdW Heterostructure programme (KCWF16) (STS measurements and DFT simulations) and the Advanced Light Source (sample growth and ARPES measurements) funded by the Director, Office of Science, Office of Basic Energy Sciences, Materials Sciences and Engineering Division, of the US Department of Energy under contract no. DE-AC02-05CH11231. Support was also provided by National Science Foundation award DMR-1508412 (DFT + U simulations), award DMR-1926004 (theoretical STS and ARPES analyses), award DMR-1507141 (electrostatic analysis) and award EFRI-1433307 (CDW model development). The work at the Stanford Institute for Materials and Energy Sciences and Stanford University (sample growth) was supported by the DOE Office of Basic Energy Sciences, Division of Material Science. Low-energy electron diffraction measurements were supported by the National Natural Science Foundation of China (grant no. 11227902). S.T. acknowledges the support by the CPSF-CAS Joint Foundation for Excellent Postdoctoral Fellows. H.R. acknowledges fellowship support from NRF, Korea through Max Planck Korea/POSTECH Research Initiatives no. 2016K1A4A4A01922028. H.-Z.T. acknowledges fellowship support from the Shenzhen Peacock Plan (grant numbers 827-000113, KQJSCX20170727100802505 and KQTD2016053112042971).

Author contributions

Y.C., W.R. and M.F.C. initiated and conceived the research. Y.C., W.R., H.-Z.T., R.L., S.K., F.L. and C.J. carried out STM/STS measurements and analyses. M.F.C. supervised STM/STS measurements and analyses. S.T., H.R., H.X. and T.J. performed sample growth and ARPES measurements. S.-K.M., Z.-X.S., J.A.S. and Z.L. supervised sample growth and ARPES measurements. M.W. performed DFT calculations and theoretical analyses. S.G.L. supervised DFT calculations and theoretical analyses. J.E.M. performed electrostatic modelling. O.R.A. and A.Y.L. provided support for development of the CDW model. Y.C., W.R. and M.F.C. wrote the manuscript with help from all authors. All authors contributed to the scientific discussion.

Competing interests

The authors declare no competing interests.

Additional information

Supplementary information is available for this paper at https://doi.org/10.1038/s41567-019-0744-9.

Correspondence and requests for materials should be addressed to M.F.C.

Peer review information *Nature Physics* thanks Matteo Calandra and the other, anonymous, reviewer(s) for their contribution to the peer review of this work.

Reprints and permissions information is available at www.nature.com/reprints.

Terms and Conditions

Springer Nature journal content, brought to you courtesy of Springer Nature Customer Service Center GmbH (“Springer Nature”).
Springer Nature supports a reasonable amount of sharing of research papers by authors, subscribers and authorised users (“Users”), for small-scale personal, non-commercial use provided that all copyright, trade and service marks and other proprietary notices are maintained. By accessing, sharing, receiving or otherwise using the Springer Nature journal content you agree to these terms of use (“Terms”). For these purposes, Springer Nature considers academic use (by researchers and students) to be non-commercial.
These Terms are supplementary and will apply in addition to any applicable website terms and conditions, a relevant site licence or a personal subscription. These Terms will prevail over any conflict or ambiguity with regards to the relevant terms, a site licence or a personal subscription (to the extent of the conflict or ambiguity only). For Creative Commons-licensed articles, the terms of the Creative Commons license used will apply.
We collect and use personal data to provide access to the Springer Nature journal content. We may also use these personal data internally within ResearchGate and Springer Nature and as agreed share it, in an anonymised way, for purposes of tracking, analysis and reporting. We will not otherwise disclose your personal data outside the ResearchGate or the Springer Nature group of companies unless we have your permission as detailed in the Privacy Policy.
While Users may use the Springer Nature journal content for small scale, personal non-commercial use, it is important to note that Users may not:

1. use such content for the purpose of providing other users with access on a regular or large scale basis or as a means to circumvent access control;
2. use such content where to do so would be considered a criminal or statutory offence in any jurisdiction, or gives rise to civil liability, or is otherwise unlawful;
3. falsely or misleadingly imply or suggest endorsement, approval , sponsorship, or association unless explicitly agreed to by Springer Nature in writing;
4. use bots or other automated methods to access the content or redirect messages
5. override any security feature or exclusionary protocol; or
6. share the content in order to create substitute for Springer Nature products or services or a systematic database of Springer Nature journal content.

In line with the restriction against commercial use, Springer Nature does not permit the creation of a product or service that creates revenue, royalties, rent or income from our content or its inclusion as part of a paid for service or for other commercial gain. Springer Nature journal content cannot be used for inter-library loans and librarians may not upload Springer Nature journal content on a large scale into their, or any other, institutional repository.
These terms of use are reviewed regularly and may be amended at any time. Springer Nature is not obligated to publish any information or content on this website and may remove it or features or functionality at our sole discretion, at any time with or without notice. Springer Nature may revoke this licence to you at any time and remove access to any copies of the Springer Nature journal content which have been saved.
To the fullest extent permitted by law, Springer Nature makes no warranties, representations or guarantees to Users, either express or implied with respect to the Springer nature journal content and all parties disclaim and waive any implied warranties or warranties imposed by law, including merchantability or fitness for any particular purpose.
Please note that these rights do not automatically extend to content, data or other material published by Springer Nature that may be licensed from third parties.
If you would like to use or distribute our Springer Nature journal content to a wider audience or on a regular basis or in any other manner not expressly permitted by these Terms, please contact Springer Nature at

onlineservice@springernature.com